

# Semantic segmentation of SEM images of lower bainitic and tempered martensitic steels

Xiaohan Bie<sup>a</sup>, Manoj Arthanari<sup>a</sup>, Evelin Barbosa de Melo<sup>a</sup>, Juancheng Li<sup>a</sup>,

Stephen Yue<sup>a\*</sup>, Salim Brahim<sup>a\*</sup>, Jun Song<sup>a\*</sup>

<sup>a</sup> Department of Mining and Materials Engineering, McGill University, Montréal, Québec H3A 0C5, Canada

## Abstract

High-strength steels constitute the foundational materials in numerous industrial applications, with lower bainite (LB) and tempered martensite (TM) emerging as two important microstructural types in this category. Recent investigations have indicated that lower bainite displays superior resistance to hydrogen embrittlement (HE) compared to tempered martensite. Researchers attribute this divergence in hydrogen embrittlement susceptibility to precipitated carbides. Studies have delineated the distinct characteristics, such as size, distribution, and orientation, of carbide precipitates within lower bainite and tempered martensite microstructures. Nevertheless, the assessment and comparison of carbides in these microstructures have primarily remained qualitative, often restricted to specific local regions lacking adequate statistical representation.

This study employs deep learning techniques to meticulously segment scanning electron microscope (SEM) images, enabling a quantitative analysis of carbide precipitates in lower bainite and tempered martensite steels possessing comparable strength. Following segmentation, carbides are investigated, and their volume

percentage, size distribution, and orientations are probed within the image dataset. Our findings reveal that lower bainite and tempered martensite exhibit comparable volume percentages of carbides, albeit with a more uniform distribution of carbides in tempered martensite. Carbides in lower bainite demonstrate a tendency for better alignment than those in tempered martensite, aligning with the observations of other researchers. However, both microstructures display a scattered carbide orientation, devoid of any discernible pattern.

Additionally, a comprehensive comparative analysis of aspect ratios and sizes of carbides in lower bainite and tempered martensite unveils striking similarities. Nonetheless, tempered martensite exhibits marginally larger aspect ratios and a higher density of precipitated carbides on average. The deep learning model achieves an impressive pixelwise accuracy of 98.0% in classifying carbide/iron matrix at the individual pixel level. The semantic segmentation derived from deep learning extends its applicability to the analysis of secondary phases in various materials, offering a time-efficient, versatile AI-powered workflow for quantitative microstructure analysis.

## 1. Introduction

High-strength steels (HSS), including ultra-high strength steels (UHSS), are distinguished by their remarkable yield strength, surpassing 210 MPa [1]. They find widespread applications in aircraft landing gears, construction, and automotive manufacturing [2-7]. By augmenting the strength of these steel alloys, it becomes possible to reduce the material's weight while still achieving the desired objectives.

Consequently, high-strength steels become an exemplary material to mitigate CO<sup>2</sup> emissions, as decreased weight leads to lower energy consumption.

The category of high-strength steels encompasses a diverse array of grades, such as High-Strength Low Alloy (HSLA) steel, Dual-Phase (DP) steel [8, 9], Martensitic (MART) steel [10], Bainitic steel [6], and various others [11]. Among the myriad steel grades, our attention is directed towards those characterized by microstructures of tempered martensite (HSLA steels) and lower bainite (Bainitic steels).

HSLA steel, a variant of carbon steel, is distinguished by the inclusion of microalloying elements such as Vanadium (V), Niobium (Nb), or Titanium (Ti) [11]. These microalloying elements, when subjected to heat treatment, activate mechanisms such as precipitate hardening [12-14] and grain refinement [15, 16]. This results in the achievement of exceptional strength levels, reaching up to 690 MPa, a significant improvement over the strength of plain carbon steels. The tempered martensite microstructure is evident in HSLA steel, produced by subjecting martensitic steels to tempering at a temperature below the eutectoid point for a specific duration. During this process, martensite undergoes decomposition as carbon atoms diffuse and precipitate, forming cementite [17].

Bainitic steels, primarily composed of bainite, form through isothermal heat treatment, known as austempering [6], and exhibit various morphologies, including lower bainite, upper bainite, and others [6]. Among these bainite morphologies, lower bainite typically forms following austempering at temperatures below 330°C and is characterized by a combination of ferrite and cementite phases [18].

Despite the distinctive nomenclature and divergent heat treatment procedures associated with tempered martensite and lower bainite, these two entities are recognized for their numerous parallels. They share similar physical attributes, encompassing hardness, modulus, yield strength, and more [6, 19, 20]. The hardness of both is subject to the influences of carbon composition and the temperature applied during heat treatment. Additionally, similarities extend to their microstructures [21], wherein both manifest laths of ferrite with finely dispersed carbide precipitates [6, 22].

Recent experimental findings [23-26] indicate a potential superior resistance to hydrogen embrittlement in the lower bainite microstructure compared to tempered martensite. Hydrogen embrittlement, a phenomenon wherein even minute quantities of hydrogen, as low as a few parts per million by weight (ppm wt%), can diffuse within steels and interact with crack tips, thereby leading to premature abrupt failures [27-29]. For instance, Jang et al. introduced hydrogen into two specimens with distinct percentages of lower bainite/tempered martensite and subsequently conducted Thermal Desorption Analysis (TDA) [26]. Their findings revealed that lower bainite structures exhibited a greater capacity for irreversibly trapping hydrogen atoms [26]. These investigations have generated substantial interest within the industry, holding significant implications for the competition between bainitic steel and HSLA in applications requiring resistance to hydrogen embrittlement.

To elucidate the reasons behind the observed differences in hydrogen embrittlement resistance, researchers have compared the microstructures of lower bainite and tempered martensite. Jang et al. attributed the heightened hydrogen embrittlement

resistance of lower bainite to the presence of more finely dispersed carbides, a deduction drawn from their analysis of precipitated carbides using Electron Channeling Contrast Imaging (ECCI) images [26]. Nanninga et al. suggested that the superior hydrogen embrittlement resistance of lower bainite can be linked to the morphologies and distributions of carbides and ferrites [25]. However, it is essential to note that the provided analyses are predominantly qualitative, raising intriguing questions about how carbide morphologies and distributions influence the hydrogen embrittlement resistivity of lower bainite and tempered martensite materials. Equally intriguing is the extent to which an increase in carbide content can enhance hydrogen embrittlement resistances.

The aforementioned puzzles underscore the necessity of quantitatively analyzing the microstructures of lower bainite and tempered martensite to gain deeper insights into how carbides influence hydrogen embrittlement resistance. Conventional methods for characterizing carbides in martensitic and bainitic steels rely on techniques such as Scanning Electron Microscopy (SEM) and Transmission Electron Microscopy (TEM), with analyses primarily qualitative [6, 26]. The absence of quantitative analysis hampers our ability to comprehensively understand these microstructures, largely due to the time-consuming nature of manually quantifying these intricate images.

Nevertheless, it is noteworthy that the advancement of deep learning (DL), a subfield of machine learning, in computer vision offers a solution to these challenges [30]. DL has demonstrated significant utility in various domains such as speech recognition, image recognition, and natural language processing [31-33]. In fact, DL has been

reported to surpass metallurgical experts in accuracy when classifying SEM images of different steel microstructures [34]. Equally impressive is the speed at which DL processes images, enabling the segmentation of hundreds of images within seconds [35]. In this study, we developed a DL workflow to efficiently segment carbides within the iron matrix in SEM images of steel. Our approach commenced with the creation of a mask to facilitate DL learning, achieved through a carbide segmentation method devised in consultation with experienced metallurgists. Subsequently, we employed the U-net architecture, a specific Convolutional Neural Network (CNN) architecture [36], to autonomously learn from our segmented data and conduct its own classification tasks. Following accuracy assessment, we conducted a thorough quantitative analysis of various carbide characteristics, encompassing carbide percentages, orientations, morphologies, and sizes, with a specific emphasis on the microstructures of lower bainite and tempered martensite.

## 2. Methodology

Among the myriad of Convolutional Neural Network (CNN) architectures, the U-Net framework has been specifically chosen for the current investigation. Introduced in 2015 by Olaf Ronneberger, Philipp Fischer, and Thomas Brox, U-Net adopts a distinctive U-shaped network architecture originally tailored for biomedical image segmentation [36]. This architecture adeptly captures both local and global information by employing an encoding path with convolutional and pooling layers for feature extraction and a decoding path for up-sampling and reconstructing the segmented image.

The incorporation of skip connections in the U-Net ensures the retention of fine-grained details during the up-sampling process. Demonstrated to be robust in segmenting images, particularly in accurately delineating complex contours, U-Net emerges as a fitting choice, given the intricate nature of interfaces between carbide precipitates and the iron matrix. Leveraging the U-Net framework, we devised a workflow for analyzing carbide precipitates in high-strength steels, with the architecture of our U-Net model delineated in Figure 1.

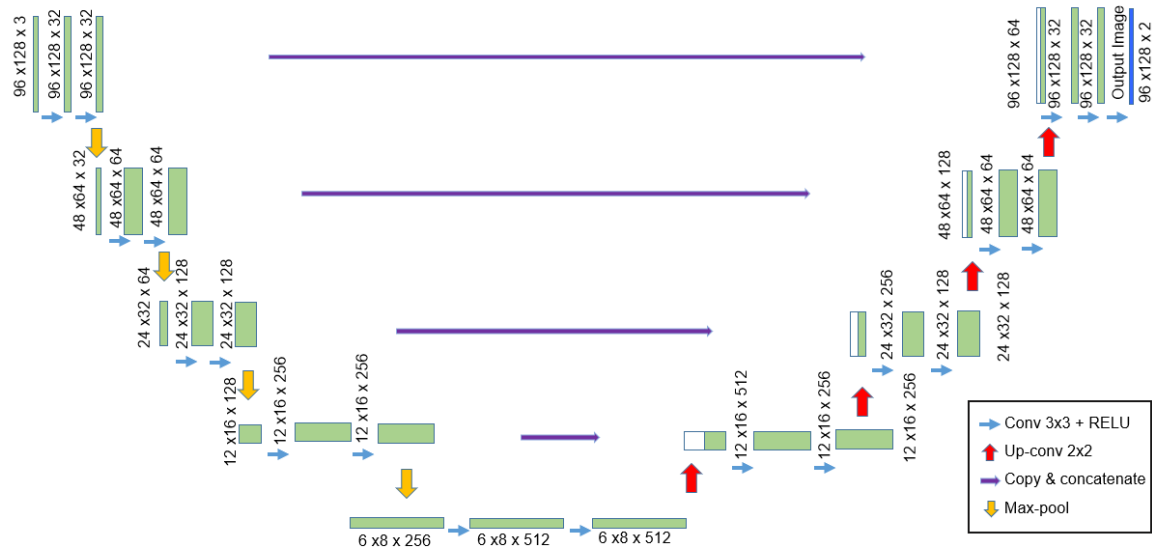


**Figure 1.** The structure of the U-Net model encompasses several key components. The initial input images are sized at 96 x 128 pixels. Within the model architecture, the 2x2 up-convolution operation is represented by the red arrow. The process of copying and concatenating feature maps is indicated by the purple arrows. Max-pooling is denoted by the orange arrows, and the 3x3 convolution operation, followed by the rectified linear unit (RELU) activation function, is represented by the blue arrows.

The aforementioned protocol comprises four fundamental stages: SEM image generation, image preprocessing, model development, and carbide analysis.

In the initial step, we obtained over 38 SEM images from our experiments. Upon careful examination of these SEM images (refer to Figure 2), it becomes evident that the dark regions correspond to the iron matrix, while the light gray regions represent carbide

precipitates, predominantly identified as cementite.

Subsequently, for the second step, masks were generated for each SEM image using Python OpenCV packages. Masks, represented in manually classified images (see Figure 3(b)), depict yellow regions as carbides and pink regions as the iron matrix. Mask generation employed a contrast-based method utilizing individual pixel intensity values. In the context of a grayscale SEM image, where 0 signifies black and 255 indicates white, a total of 153600 pixels in a 480x320 pixel image were assigned values ranging from 0 to 255. These values corresponded to varying intensities, with darker shades associated with lower numerical values compared to lighter shades.

To identify carbides, 16 masks were generated for each SEM image, each with a threshold selected from a set of 16 benchmark intensity values. If a pixel's intensity value exceeded the threshold, it was classified as a carbide and colored yellow; otherwise, it was identified as part of the iron matrix and colored pink. An iterative process in collaboration with experienced metallurgists was employed to select the most accurate mask for distinguishing between carbide and non-carbide areas across all SEM images in the study (cf. Figure 3(a)-(b)).

Following mask creation, both the original images and their corresponding masks were cropped into smaller 480x640 pixel images. A dataset comprising 1094 cropped images, depicting either lower bainite or tempered martensite microstructures, was generated. For efficient training, these images were resized to 96x128 pixels.

In the third stage, the DL model underwent training and testing, utilizing a sub-partitioned dataset into training, validation, and test sets. The training set was employed



for model construction, the validation dataset for parameter tuning, and the test set for model evaluation. The DL model was trained using pairs of cropped original images and masks.

In the final stage, a quantitative analysis of carbide morphologies, including volumetric percentages, orientations, aspect ratios, and sizes in SEM images, was conducted.

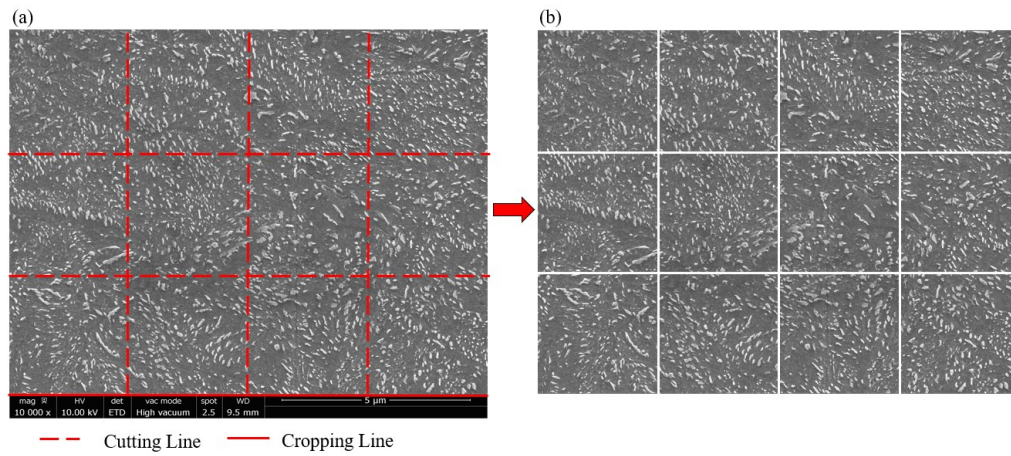


**Figure 2** Original SEM images (a) and cropped images (b).

## 3. Results and Discussion

### 3.1 Deep Learning Prediction and Accuracy Assessment

#### 3.1.1. Loss and Accuracy

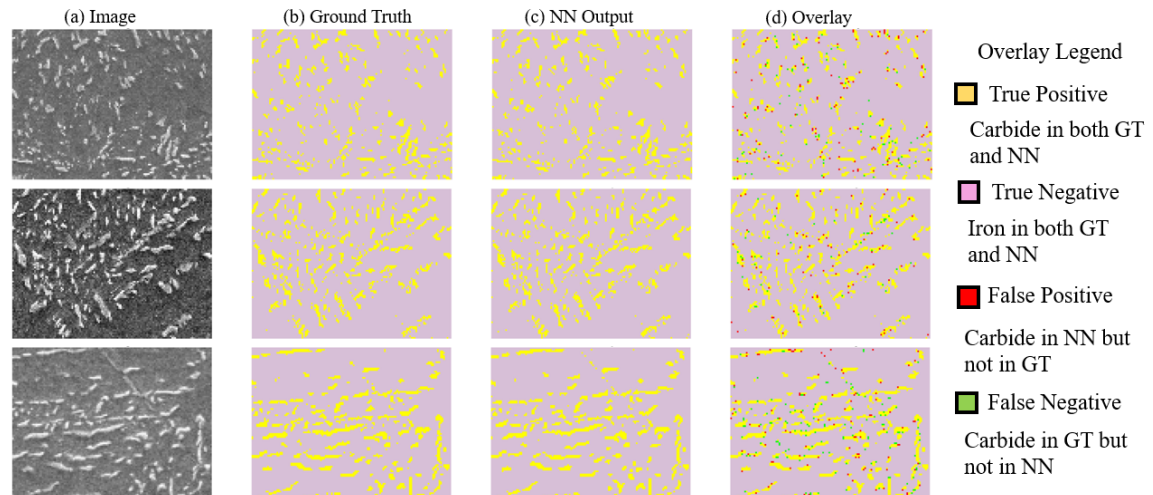


**Figure 3** (a) Original SEM images and (b) created masks (ground truth), (c) neural network classifications, (d) Overlay of results with legend displayed.

Figures 3(a) and (b) depict cropped images and corresponding ground truth masks generated in Step 1. Carbides smaller than 30 pixels, considered as background noise, were categorized as part of the iron background in the masks. In Step 2, our U-Net model underwent training using these image-mask pairs. The predictions made by our U-Net model for the original SEM images (Figure 3(a)) are presented in Figure 3(c). The performance of our model is assessed through two parameters: pixel accuracy and Intersection over Union (IoU). Pixel accuracy quantifies correctly predicted pixels relative to the total number of pixels, while the loss function, a crucial aspect in machine learning, denotes the disparity between predicted and true values, guiding the

optimization process. For classification tasks, the widely utilized loss function, cross-entropy, proves particularly effective. It assesses the dissimilarity between the predicted probability distribution and the authentic distribution of the target variable. The binary cross-entropy loss function is computed as follows:

$$Loss = -\frac{1}{output\ size} \sum_{i=1}^{output\ size} y_i \cdot \log \hat{y}_i + (1 - y_i) \log (1 - \hat{y}_i) \quad (1)$$

Here,  $y_i$  represents the label, assuming a value of 1 for a carbide pixel and 0 for an iron background pixel, while  $\hat{y}_i$  denotes the predicted probability of point  $i$  being a carbide. Upon closer examination of this equation, it becomes evident that, for each carbide point ( $y_i=1$ ), the loss incorporates the logarithm of  $\hat{y}_i$ , signifying the log probability of it being a carbide. Conversely, for each iron background point ( $y_i=0$ ), the loss incorporates  $\log(1-\hat{y}_i)$ . In binary classification, the cross-entropy loss manifests as the average negative logarithm of the predicted probability for the true class.

Focusing on the  $i$ th pixel in the summation, if it corresponds to true carbide ( $y_i=1$ ), the inclusion of  $-\log(y_i)$  in the summation occurs. Notably, as the predicted probability  $y_i$  approaches 1, the resulting loss values diminish, indicating a stronger alignment between prediction and truth. Conversely, if the  $i$ th pixel represents true iron ( $y_i=0$ ), the summation incorporates  $-\log(1-y_i)$ . It is essential to observe that as the predicted probability  $y_i$  approaches 0, the resulting loss diminishes, favoring higher probabilities for accurate categorization and lower probabilities for erroneous classification. The minimization of cross-entropy loss is crucial in optimizing the model's precision in predictions, facilitating a more effective approximation of the genuine distribution of the target variable. This optimization process often employs techniques such as gradient descent [37], enabling the adjustment of model parameters to seek the optimal configuration that minimizes loss functions.

Supplementary material S2 provides insights into the accuracy and loss trajectories

throughout the training process, where both figures utilize the number of epochs as the x-axis. In the context of machine learning, an epoch signifies a complete traversal through the training data. Notably, the figures illustrate a convergence of both training and validation accuracies after 10 epochs. In our study, a deliberate choice was made to conduct a total of 60 epochs to ensure the convergence of accuracy. Remarkably, at the conclusion of these 60 epochs, the training dataset achieves an accuracy of 98.3%, while the validation dataset attains an equally remarkable accuracy of 98.0% (refer to Figure S1). Additionally, the model's performance was assessed on unseen data (test dataset), resulting in a test accuracy of 98.0%. Regarding the loss values, they significantly decrease to 0.041 for the training dataset and 0.047 for the validation dataset (cf. Figure S1), indicating a harmony between predictions and true values and highlighting a highly accurate model performance.

For error analysis, a selection of images was meticulously chosen to scrutinize instances of inaccurate predictions. Figure 3 (d) displays overlaid pixels that were predicted incorrectly. The yellow areas represent carbides in both the Neural Network (NN) predictions and our masks, while the pink areas correspond to iron in both the masks and NN predictions. Furthermore, the green pixels indicate false negatives, where the NN classifies regions as the iron matrix, but they are carbides according to the masks. Conversely, the red pixels depict false positives, where the NN identifies regions as carbides, but they are part of the iron matrix according to the masks. These prediction errors are primarily concentrated at the periphery of the carbides, which area presents a challenge even for experienced metallurgists to distinguish between carbides and the

iron matrix. Nonetheless, within this context, our DL model demonstrates reasonably accurate predictions.

### 3.1.2. Intersection over Union (IoU)

To rigorously assess the accuracy of our model, we conducted an evaluation based on Intersection over Union (IoU) specifically applied to carbides. IoU is defined as the ratio of the intersection between predicted carbides and the ground truth of carbides (refer to Supplement S2(d)) over the union of the prediction and ground truth (refer to Supplement S2(e)) [38]. IoU stands as an important metric for comparing the similarity between two shapes [39]. One notable advantage of the IoU method lies in its normalization of shape comparison, ensuring that IoU values remain invariant to the scale of the problem under examination. This characteristic establishes IoU as a reliable and consistent metric for comparing the similarity between two shapes, irrespective of the scale of the problem. The favorable properties of IoU have led to its widespread utilization in segmentation [40, 41] and object detection [42, 43].

To perform the IoU calculation, it is imperative to grasp the essence of two key terms: True Positive (TP) and False Positive (FP). A True Positive occurs when the model correctly identifies a pixel as belonging to carbide, aligning with the mask's assertion that the pixel indeed represents carbide. Conversely, a False Positive arises when the model erroneously classifies a pixel as carbide, disregarding the mask's affirmation that it pertains to the iron background. A False Negative occurs when the model fails to identify a pixel as belonging to carbide, despite the ground truth mask indicating its

presence. Therefore, the term IoU can be calculated by:

$$IoU = \frac{TP}{TP + FP + FN} \quad (2)$$

Where TP signifies True Positive, FP represents False Positive, and FN stands for False Negative. IoU values are computed for each image, and the outcomes are documented in Figure 4.

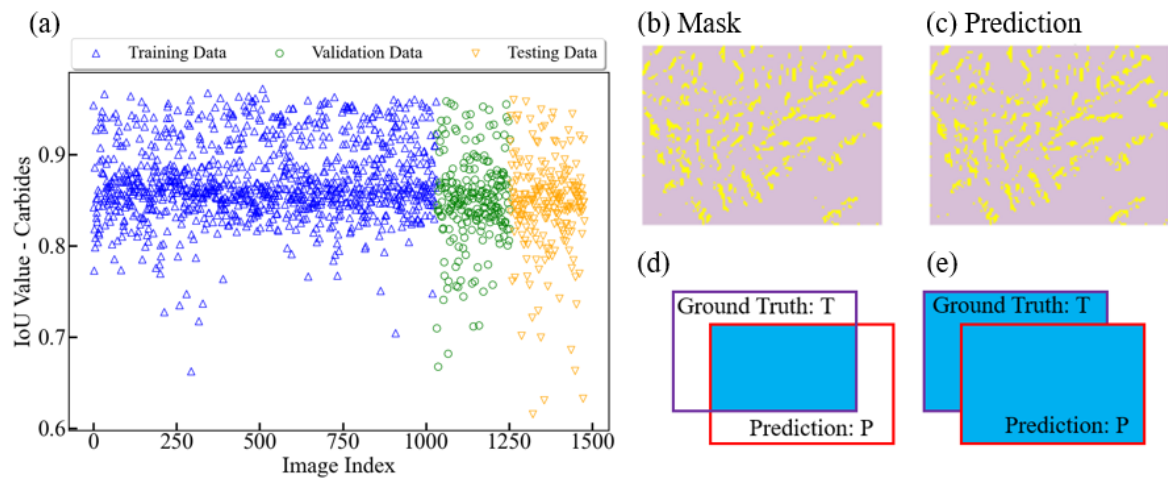


**Figure 4** The Intersection over Union (IoU) graph illustrates the relationship between IoU values and their corresponding image numbers. The x-axis corresponds to the image's index, while the y-axis indicates the IoU value for each respective image.

As depicted in Figure 4, the IoU values for both the validation and test sets closely resemble those of the training set, indicating low variance. This suggests that our model exhibits effective generalization, accurately discerning secondary phases from SEM images. While the majority of cropped images yield IoU values above 0.85, instances exist where IoU values hover around 0.7. This may be attributed to the limited number of images in the training dataset, potentially impacting the model's performance in specific cases. We have selectively presented figures based on their lower IoU values in Figure 5. In Figure 5 (a), the IoU value is calculated to be 0.68, while in Figure 5 (b), it is 0.69. Similarly, for Figure 5 (c), the IoU value is determined to be 0.69. Figures 5 (d-e) present the original SEM images corresponding to the overlaid masks in Figure 5 (a-c). Figures 5 (g-i) showcase the superimposed masks (Figure 5(a-c)) alongside the

original SEM images (Figure 5 (d-f)).

Upon observation, the green areas are identified as false negatives, indicating misclassification as iron in our DL model despite being classified as carbides in the mask. Conversely, the red areas denote false positives, where the mask designates them as iron, but our DL prediction identifies them as carbides. Examination of falsely predicted pixels reveals that these errors primarily occur at the periphery of the carbides. Notably, in image (a), the microstructures exhibit significant complexity, challenging accurate determination even for experienced metallurgists. For Figure 5 (c), areas identified as false positives are, upon careful examination, regions of carbides, indicating accurate DL prediction. In this specific image, selecting all carbides without imperfections using the contrast selection method is challenging. In this regard, our DL model outperforms manual efforts.

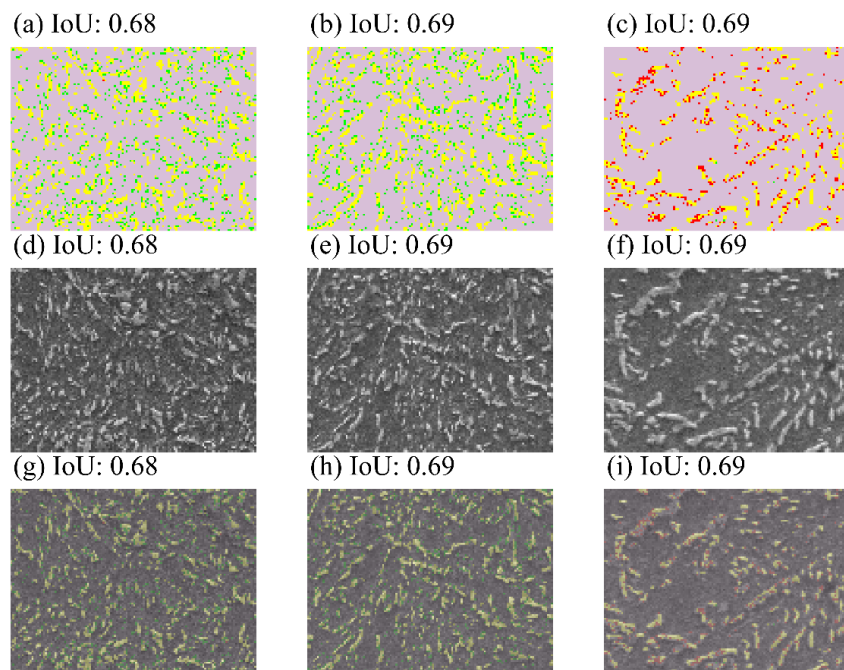


**Figure 5** (a-c) A superimposition of masks and predictions for images characterized by low IoU values. The yellow areas delineate carbides present in both the manually selected mask and DL predictions. The pink areas correspond to the iron background, consistently identified in both the mask and DL prediction. Green areas indicate false negatives, representing regions initially designated as carbides in the mask but incorrectly classified as iron in our DL model. The red areas denote false positives, where the mask

designates them as iron, yet our DL prediction identifies them as carbides. (d-e) correspond to the SEM images of (a-c).

### 3.2 Comparisons of Carbides in Lower Bainite and Tempered Martensite

Having successfully isolated the carbides, our focus shifted to characterizing their percentage and orientations. In Figure 6 (a), the DL model adeptly discerned the carbides, enabling the determination of their percentage by meticulously dividing the count of carbide pixels by the total number of pixels within the image. The subsequent processing is illustrated in Figure 6 (b), where each carbide was encapsulated.

To construct the enclosing box for the carbides, our initial step involved identifying carbide contours using border-following algorithms [44] implemented by OpenCV [45]. These algorithms facilitated the extraction of a sequence of coordinates or chain codes from the border between the connected component of carbide pixels (represented by 1) and the connected component of iron pixels (represented by 0).

Subsequently, we determined the rotated rectangle with the minimum area that encompasses the identified contours. Among the sides of this rectangle, the longer edge was considered the principal axis. To ascertain the orientation of the principal axis relative to the horizontal direction (rightward), we calculated the angle within a range of -90 to 90 degrees (see Figure 6(c) and (d)). Carbide regions, distinguished by their yellow hue and encompassing an area smaller than 30 pixels, were classified as noises and intentionally excluded from being enclosed in rectangular boundaries.

Figure 6 presents a cropped image from our dataset. For comprehensive statistical insights, we computed the data for each image and consolidated the results, as depicted in Figure 7. In Figure 7(a), each dot represents the calculated carbide percentage relative to the image number. Red circles denote bainite, while blue triangles represent martensite. We also determined and plotted the average percentage of bainite and martensite. Upon analyzing the data in Figure 7 (a), it becomes apparent that the carbide percentage data in lower bainite exhibits greater dispersion compared to that in



tempered martensite. The standard deviation (STD) for lower bainite is 0.02, whereas the STD for tempered martensite is 0.01. However, the average carbide percentages in lower bainite and tempered martensite exhibit remarkable similarity, both being 0.13. This leads to the conclusion that while the number of precipitated carbides does not significantly differ between these two materials, carbides in tempered martensite display a more uniform distribution than those in lower bainite.

In Figure 7 (b), we quantified the alignment factor to characterize carbide orientations. For each carbide, we calculated the angle between its orientation and the horizontal line. The angle ranges from  $-90^\circ$  to  $90^\circ$  (cf. Figure 6 (c-d)) and was divided into 18 intervals. The interval with the highest carbide count among the 18 intervals is identified by its left boundary (denoted as  $a$ ) and right boundary (denoted as  $b$ ). The alignment factor, denoted as  $k$ , is defined as the ratio of the carbide count within the maximum interval to the total count across the entire range. The alignment factor is calculated as:

$$k = \frac{\int_a^b f(x)dx}{\int_{-90^\circ}^{90^\circ} f(x)dx} \quad (3)$$

Where The function  $f(x)$  represents the orientation density over the entire range. We divide this range into small intervals, denoted by  $a$  and  $b$ . For instance, if  $a = -90$  and  $b = -80$ , or  $a = 80$  and  $b = 90$ , we select an interval of 10 degrees. We partitioned the entire range into 18 parts, meaning that  $a$  takes values of  $-90, -80, -70, -60, -50$ , and so on up to  $50, 60, 70, 80$ , and  $90$ . After dividing the range into these subintervals, we obtain 18 ratios for each figure. The maximum ratio among the 18 ratios is determined to be  $k$ , for that specific image.

The outcomes reveal that the average alignment factor in lower bainite is 0.38, as indicated by the red line in Figure 7 (b), while the corresponding value for tempered martensite is 0.34, represented by the blue dotted line in Figure 7 (b). The standard

deviations (STD) of  $k$  are at comparable levels, with lower bainite at 0.07 and tempered martensite at 0.05. The higher alignment factor observed in lower bainite suggests a more pronounced alignment of carbides compared to tempered martensite. This discovery aligns with established industrial techniques utilized to differentiate lower bainite from tempered martensite [6]. Previous studies have observed that, unlike tempered martensite, carbides in lower bainite tend to exhibit a single variant with an angle of approximately  $60^\circ$  relative to the "growth direction" of the ferrite plate [46, 47].

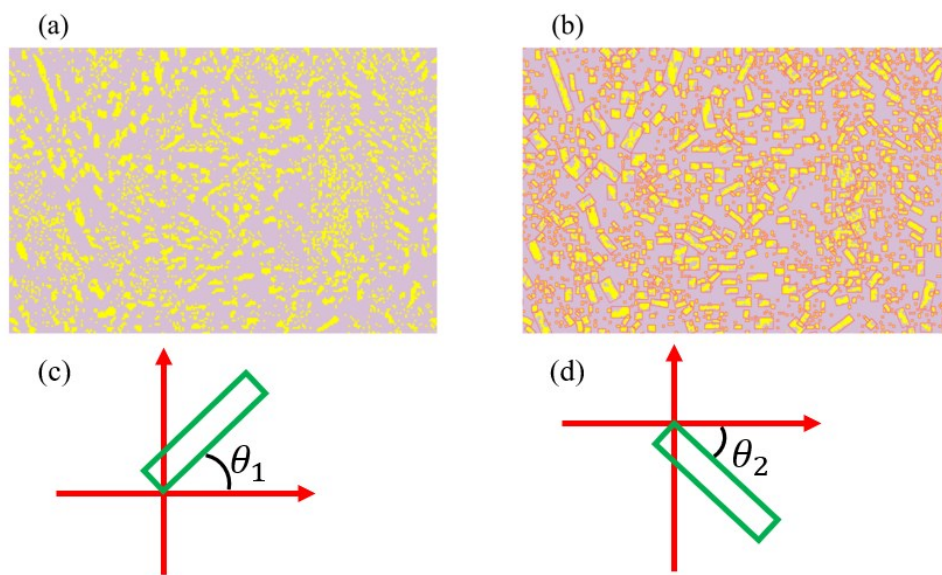


**Figure 6** (a) Neural Network (NN) classifications of carbides and the iron matrix, (b) highlighting carbide areas for orientation characterization (regions with areas smaller than 30 pixels are considered background noise and are intentionally excluded from being enclosed within rectangles), (c) displays carbides with angles ranging between 0 and 90 degrees, while (d) depicts carbides with angles ranging from -90 to 0 degrees.

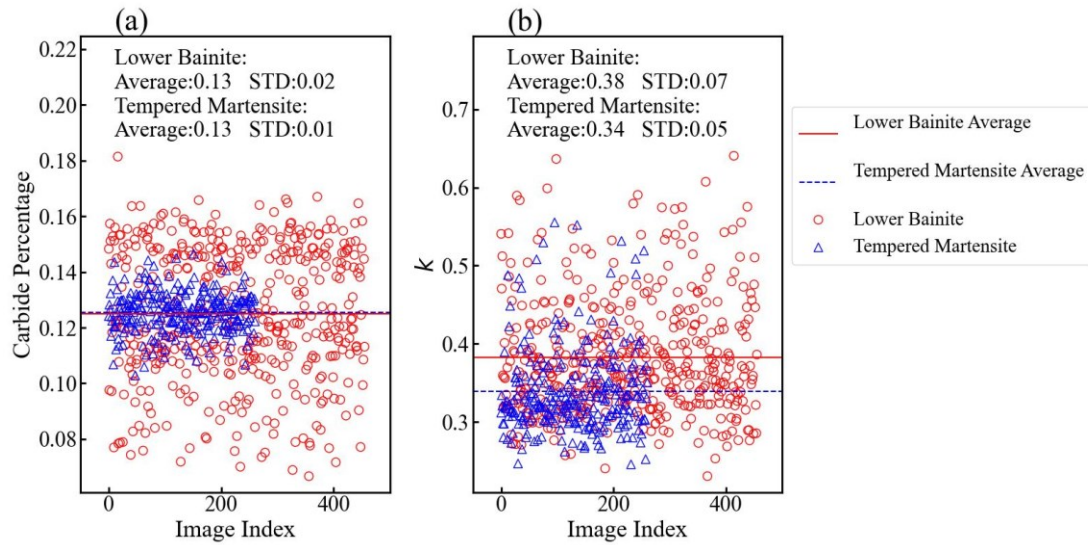


**Figure 7** (a) the relationship between carbide percentage and image index and (b) the alignment factor  $k$  of carbides versus image index in each image.

Following this, we computed the aspect ratios of each carbide, and the outcomes are depicted in Figure 8. This involved a meticulous calculation where we divided the length of the longer edge by that of the shorter edge of the corresponding rectangle. Collecting the data from all the SEM images, we presented the comprehensive results in Figure 8. Each blue triangle corresponds to a data point representing tempered martensite, while each red triangle represents a carbide data point in lower bainite. Mean values of the aspect ratios, along with standard deviations, were also computed. The overall average aspect ratio for lower bainite was determined to be 1.62, the same as the mean value for tempered martensite, which also stood at 1.62. The standard deviations for these two materials were calculated as 0.56 for lower bainite and 0.57 for tempered martensite, respectively. Based on the collected data, it is evident that the aspect ratios of carbides in these two materials align within a similar range, highlighting the fact that they have similar morphologies, even from a quantitative standpoint.

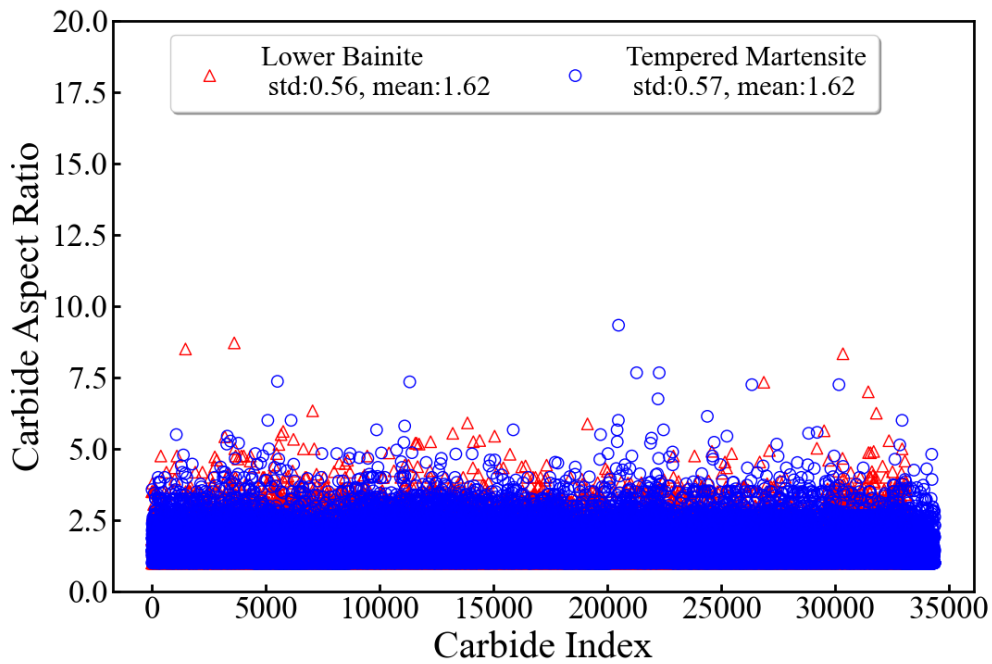


**Figure 8**, the aspect ratios of carbides in lower bainite are represented by red triangles, and those in tempered martensite are denoted by blue triangles. The mean aspect ratios for both lower bainite and tempered martensite are calculated to be 1.62. The standard deviations for lower bainite and tempered martensite are measured as 0.56 and 0.57, respectively. These values closely align, emphasizing the similarity in aspect ratios between carbides in lower bainite and tempered martensite.

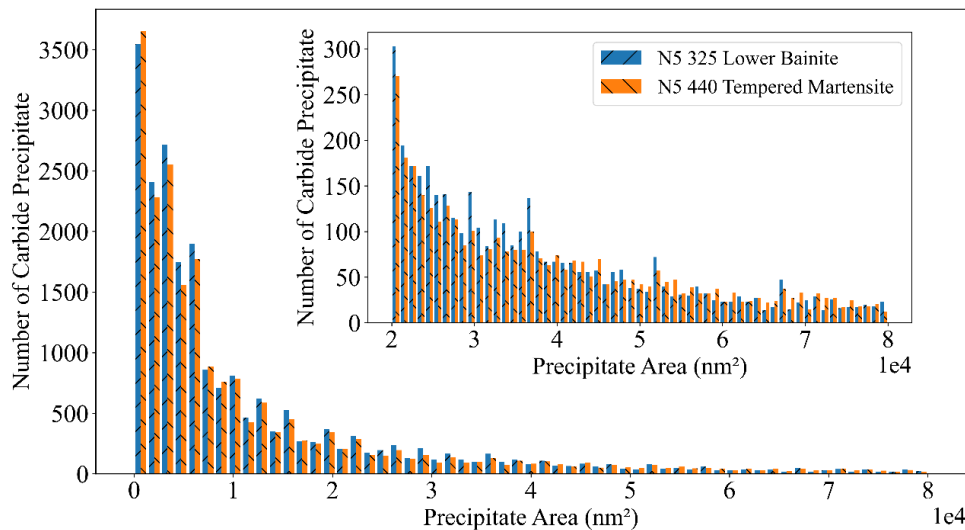


**Figure 9** The size distributions of carbides in lower bainite and tempered martensite are depicted in blue and orange regions, respectively. Significantly, precipitated carbides with areas exceeding 2 nm<sup>2</sup> are magnified and presented within a distinct rectangle to enhance visibility and facilitate examination.

To facilitate a comprehensive comparison between carbides in lower bainite and tempered martensite, we also conducted an examination of their respective sizes. To ensure precise size computations, the small, cropped images were amalgamated to mitigate any errors stemming from the initial cropping of the carbides. An illustrative example of a merged SEM image can be found in Supplementary S4. A collection of SEM images spanning 11 magnifications, ranging from 5000X to 20000X, was acquired for both lower bainite and tempered martensite. The carbide data from all images were compiled, and the areas of the carbides were calculated in nanometer squared units. These carbide size results were then aggregated and presented in Figure 9. The analysis reveals a higher prevalence of finely dispersed small carbides in tempered martensite compared to lower bainite. However, the overall difference in carbide sizes between the two materials is not deemed significant.

The comparative analysis of carbide precipitates in lower bainite and tempered martensite highlights minimal disparities between these two materials. The findings underscore the striking similarities in carbide percentages between tempered martensite and lower bainite. Notably, carbide percentages in tempered martensite exhibit smaller standard deviations, indicative of a more uniform distribution of carbides within this material. In terms of orientations, carbides in lower bainite display a slightly greater alignment than those in tempered martensite. Regarding morphologies, there are no substantial differences observed in the aspect ratios of the carbides. However, in terms of sizes, tempered martensite exhibits a higher prevalence of finely dispersed carbides, although the discrepancy is not considered substantial.

The outcomes of this investigation emphasize the considerable potential of deep learning as a robust approach for phase analysis in material characterizations. With its exceptional time efficiency and elevated accuracy, deep learning outperforms human experts in this specific domain. The deployment of deep learning as a tool for phase classification in steels, subsequent to rigorous training, firmly solidifies its standing as an invaluable asset within the field.

## 6 Conclusion

In the course of this investigation, we designed a workflow tailored for a thorough quantitative analysis of precipitates in scanning electron microscopy (SEM) images of steels, with a particular emphasis on carbide precipitates in lower bainite and tempered martensite. Following a comprehensive examination, we have unveiled the considerable promise of employing deep learning algorithms for the analysis of microstructural characteristics in lower bainite and tempered martensite. The key discoveries are encapsulated as follows:

1. We engineered a deep learning model proficient in categorizing carbides and the iron matrix in SEM images of lower bainite and tempered martensite. Our DL model demonstrated exceptional performance, achieving a pixelwise accuracy of 98.0% in discerning between carbides and non-carbides at the pixel level.
2. The success of deep learning in segmenting phases within steels lays the groundwork for a flexible AI-driven workflow, enhancing the efficiency of quantitative microstructure analysis. Our established workflow is ready for

seamless adaptation to analyze precipitates in diverse steel systems.

3. A comprehensive statistical examination of carbide volumetric percentages in lower bainite and tempered martensite was undertaken. Our analysis revealed a noteworthy similarity in the volume percentage of carbides between lower bainite and tempered martensite, highlighting a discernible difference in the more uniform distribution of carbides within the tempered martensite microstructure.
4. Carbides within lower bainite demonstrated a higher level of alignment compared to those in tempered martensite, aligning with observations from prior experimental studies. However, it is crucial to emphasize that carbide orientations in both lower bainite and tempered martensite exhibited notable scattering, devoid of any distinct alignment pattern.
5. Our findings indicate a notable resemblance in the aspect ratios and sizes of carbides between the two structures. Remarkably, tempered martensite, on average, exhibited slightly larger aspect ratios.

## 7 References

- [1] J. Galán, L. Samek, P. Verleysen, K. Verbeken, Y. Houbaert, Advanced high strength steels for automotive industry, *Revista de metalurgia* 48(2) (2012) 118.
- [2] S. Jenkins, Landing gear design and development, *Proceedings of the Institution of Mechanical Engineers, Part G: Journal of Aerospace Engineering* 203(1) (1989) 67-73.
- [3] R. Kuziak, R. Kawalla, S. Waengler, Advanced high strength steels for automotive industry, *Archives of civil and mechanical engineering* 8(2) (2008) 103-117.
- [4] T. Kamo, R. Ando, M. Sasaki, T. Suzuki, Y. Watanabe, Ultra high strength steel for sustainable building structures, *NSSMC Technical Report 10* (2015) 65-69.
- [5] F. Badkoobeh, H. Mostaan, M. Rafiei, H.R. Bakhsheshi-Rad, F. Berto, Microstructural characteristics and strengthening mechanisms of ferritic–martensitic dual-phase steels: a review, *Metals* 12(1) (2022) 101.
- [6] H.K.D.H. BHADSHIA, BAINITE IN STEELS, (2015).
- [7] R. Wanhill, R. Byrnes, C. Smith, Stress corrosion cracking (SCC) in aerospace vehicles, *Stress Corrosion Cracking* (2011) 608-650.
- [8] M. Rashid, Dual phase steels, *Annual Review of Materials Science* 11(1) (1981) 245-266.
- [9] G. Speich, Dual-phase steels, *ASM International, Metals Handbook. Tenth Edition. 1* (1990) 424-429.
- [10] T. Hilditch, T. De Souza, P. Hodgson, Properties and automotive applications of advanced high-strength steels (AHSS), *Welding and joining of advanced high strength steels (AHSS)*, Elsevier2015, pp. 9-28.
- [11] C. Garcia, High strength low alloyed (HSLA) steels, *Automotive Steels*, Elsevier2017, pp. 145-167.
- [12] M.-Y. Chen, M. Gouné, M. Verdier, Y. Bréchet, J.-R. Yang, Interphase precipitation in vanadium-alloyed steels: Strengthening contribution and morphological variability with austenite to ferrite transformation, *Acta materialia* 64 (2014) 78-92.
- [13] M. Charleux, W. Poole, M. Militzer, A. Deschamps, Precipitation behavior and its effect on strengthening of an HSLA-Nb/Ti steel, *Metallurgical and Materials Transactions A* 32 (2001) 1635-1647.
- [14] W. Lee, S. Hong, C. Park, K. Kim, S. Park, Influence of Mo on precipitation hardening in hot rolled HSLA steels containing Nb, *Scripta materialia* 43(4) (2000) 319-324.
- [15] J. Majta, K. Muszka, Mechanical properties of ultra fine-grained HSLA and Ti-IF steels, *Materials Science and Engineering: A* 464(1-2) (2007) 186-191.
- [16] J.R. Paules, Developments in HSLA steel products, *JOM* 43(1) (1991) 41-44.
- [17] H. Bhadeshia, R. Honeycombe, *Steels: microstructure and properties*, Butterworth-Heinemann2017.
- [18] I. Chakrabarty, Heat Treatment of Cast Irons, *Comprehensive Materials Finishing* 2 (2017) 246-287.
- [19] R. Grange, C. Hribal, L. Porter, Hardness of tempered martensite in carbon and low-alloy steels, *Metallurgical transactions A* 8 (1977) 1775-1785.
- [20] J.M. Tartaglia, K.A. Lazzari, G.P. Hui, K.L.J.M. Hayrynen, M.T. A, A comparison of mechanical properties and hydrogen embrittlement resistance of austempered vs quenched and tempered



4340 steel, 39(3) (2008) 559-576.

- [21] R.E. Smallman, A. Ngan, Physical metallurgy and advanced materials, Elsevier 2011.
- [22] H.K.D.H. Bhadeshia, Steels for Rails, Novel, in: K.H.J. Buschow, R.W. Cahn, M.C. Flemings, B. Ilshner, E.J. Kramer, S. Mahajan, P. Veyssi re (Eds.), Encyclopedia of Materials: Science and Technology, Elsevier, Oxford, 2002, pp. 1-7.
- [23] J.M. Tartaglia, K.A. Lazzari, G.P. Hui, K.L. Hayrynen, A comparison of mechanical properties and hydrogen embrittlement resistance of austempered vs quenched and tempered 4340 steel, Metallurgical and Materials Transactions A 39(3) (2008) 559-576.
- [24] D.E. Hyer-Peterson, Hydrogen embrittlement of 4340 with martensitic and bainitic microstructures for fastener applications, Colorado School of Mines 2019.
- [25] N. Nanninga, J. Grochowksi, L. Heldt, K. Rundman, Role of microstructure, composition and hardness in resisting hydrogen embrittlement of fastener grade steels, Corrosion Science 52(4) (2010) 1237-1246.
- [26] J.W. Jo, H.J. Seo, B.-I. Jung, S. Choi, C.S. Lee, Effect of bainite fraction on hydrogen embrittlement of bainite/martensite steel, Materials Science and Engineering: A 814 (2021) 141226.
- [27] R. Oriani, Hydrogen embrittlement of steels, Annual review of materials science 8(1) (1978) 327-357.
- [28] M. Alexander Stopher, P.E.J. Rivera-Diaz-del-Castillo, Hydrogen embrittlement in bearing steels, Materials Science and Technology 32(11) (2016) 1184-1193.
- [29] O. Barrera, D. Bombac, Y. Chen, T. Daff, E. Galindo-Nava, P. Gong, D. Haley, R. Horton, I. Katzarov, J.J.J.o.M.S. Kermode, Understanding and mitigating hydrogen embrittlement of steels: a review of experimental, modelling and design progress from atomistic to continuum, (2018) 1-40.
- [30] A. Voulodimos, N. Doulamis, A. Doulamis, E. Protopapadakis, Deep Learning for Computer Vision: A Brief Review, Computational Intelligence and Neuroscience 2018 (2018) 1-13.
- [31] U. Kamath, J. Liu, J. Whitaker, Deep learning for NLP and speech recognition, Springer 2019.
- [32] L. Deng, G. Hinton, B. Kingsbury, New types of deep neural network learning for speech recognition and related applications: An overview, 2013 IEEE international conference on acoustics, speech and signal processing, IEEE, 2013, pp. 8599-8603.
- [33] H. Fujiyoshi, T. Hirakawa, T. Yamashita, Deep learning-based image recognition for autonomous driving, IATSS research 43(4) (2019) 244-252.
- [34] M. Larmuseau, M. Sluydts, K. Theuwissen, L. Duprez, T. Dhaene, S. Cottenier, Race against the Machine: can deep learning recognize microstructures as well as the trained human eye?, Scripta Materialia 193 (2021) 33-37.
- [35] F. Chollet, Deep learning with Python, Simon and Schuster 2021.
- [36] O. Ronneberger, P. Fischer, T. Brox, U-Net: Convolutional Networks for Biomedical Image Segmentation, arXiv pre-print server (2015).
- [37] S. Ruder, An overview of gradient descent optimization algorithms, arXiv preprint arXiv:1609.04747 (2016).
- [38] A. Rosebrock, Intersection over Union (IoU) for object detection, 2016.
- [39] H. Rezatofighi, N. Tsoi, J. Gwak, A. Sadeghian, I. Reid, S. Savarese, Generalized intersection over union: A metric and a loss for bounding box regression, Proceedings of the IEEE/CVF conference on computer vision and pattern recognition, 2019, pp. 658-666.
- [40] A. Bihani, H. Daigle, J.E. Santos, C. Landry, M. Prodanovi c, K. Milliken, MudrockNet: Semantic

segmentation of mudrock SEM images through deep learning, *Computers & Geosciences* 158 (2022) 104952.

[41] B. Zhou, H. Zhao, X. Puig, S. Fidler, A. Barriuso, A. Torralba, Scene parsing through ade20k dataset, *Proceedings of the IEEE conference on computer vision and pattern recognition*, 2017, pp. 633-641.

[42] T.-Y. Lin, M. Maire, S. Belongie, J. Hays, P. Perona, D. Ramanan, P. Dollár, C.L. Zitnick, Microsoft coco: Common objects in context, *European conference on computer vision*, Springer, 2014, pp. 740-755.

[43] M. Everingham, L. Van Gool, C.K. Williams, J. Winn, A. Zisserman, The pascal visual object classes (voc) challenge, *International journal of computer vision* 88(2) (2010) 303-338.

[44] S. Suzuki, K. be, Topological structural analysis of digitized binary images by border following, *Computer Vision, Graphics, and Image Processing* 30(1) (1985) 32-46.

[45] G. Bradski, *The OpenCV Library*, Dr. Dobb's Journal of Software Tools (2000).

[46] K.i. Shimizu, T. Ko, Z. Nishiyama, Transmission electron microscope observation of the bainite of carbon steel, *Transactions of the Japan Institute of Metals* 5(4) (1964) 225-230.

[47] G. Speich, Growth Kinetics of Bainite in a Three Per Cent Chromium Steel, *Decomposition of Austenite by Diffusional Processes: Proceedings of a Symposium Held in Philadelphia, Pennsylvania, October 19, 1960, Under the Sponsorship of the Ferrous Metallurgy Committee of the Institute of Metals Division, the Metallurgical Society, American Institute of Mining, Metallurgical, and Petroleum Engineers, Interscience Publishers, 1962, p. 353.*